Electronic Supplementary Material (ESI) for Materials Horizons.

Capping layer enabled controlled fragmentation of two-dimensional materials by cold drawing

Ming Chen[1,2,*,§], Dong Li[3,§], Yuxin Hou[1,2,§], Mengxi Gu[1,2], Qingsheng Zeng[4], De Ning[1,2], Weimin Li[1,2], Xue Zheng[1,2], Yan Shao[1,2], Zhixun Wang[5,*],Juan Xia[6], Chunlei Yang[1,2,*], Lei Wei[5,*] and Huajian Gao[3,7,*]

[1]Shenzhen Institute of Advanced Technology, Chinese Academy of Sciences, Shenzhen 518055, China

[2]University of Chinese Academy of Sciences, Beijing 100049, China

[3]School of Mechanical and Aerospace Engineering, Nanyang Technological University, Singapore 639798, Singapore

[4]Center for Programmable Materials, School of Materials Science and Engineering, Nanyang Technological University, Singapore 639798, Singapore

[5]School of Electrical and Electronic Engineering, Nanyang Technological University, Singapore 639798, Singapore

[6]Institute of Fundamental and Frontier Sciences, University of Electronic Science and Technology of China, Chengdu, China

[7]Institute of High Performance Computing, A*STAR, Singapore 138632, Singapore

*Corresponding authors: ming.chen2@siat.ac.cn. zhixun.wang@ntu.edu.sg, cl.yang@siat.ac.cn, wei.lei@ntu.edu.sg, huajian.gao@ntu.edu.sg.

[§]These authors contributed equally to this work

Keywords: cold-drawing, two-dimensional materials, capping layer, necking, flexible electronics.

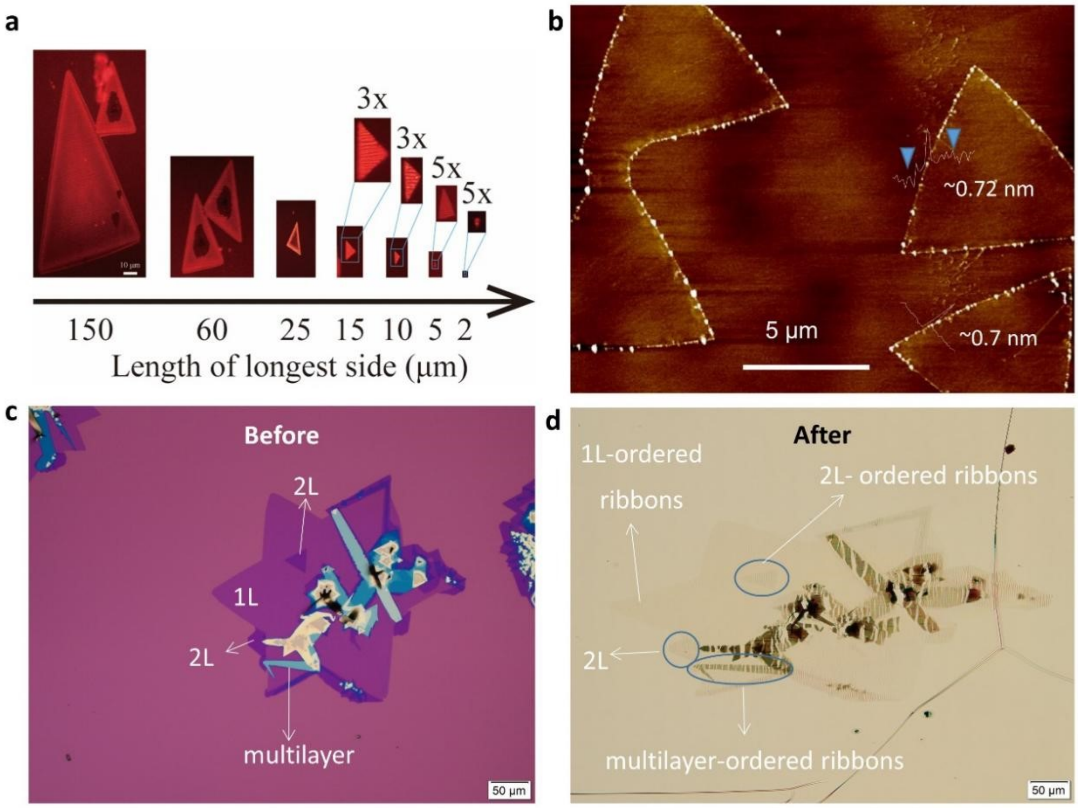

Figure S1. (a) Ordered fragmentation in WS_2 flakes with different sizes. Ordered fragmentation was observed in flakes with different lateral dimensions. The scale bar applies to all images except insets. (b) The thickness of the monolayer WS_2 film revealed by atomic force microscopy (AFM) image. Monolayer, double layer, and multilayer WS_2 film (c) before cold drawing and (d) after cold drawing. Monolayer, double layer, and multilayer WS_2 film are all fragmented into ordered ribbons. Double-layer ribbons are wider than monolayer ribbons, while multilayer ribbons have the largest width. The experimental observation is consistent with the theory, which describes that the fragmentation size is proportional to the thickness (number of layers) of WS_2 film.

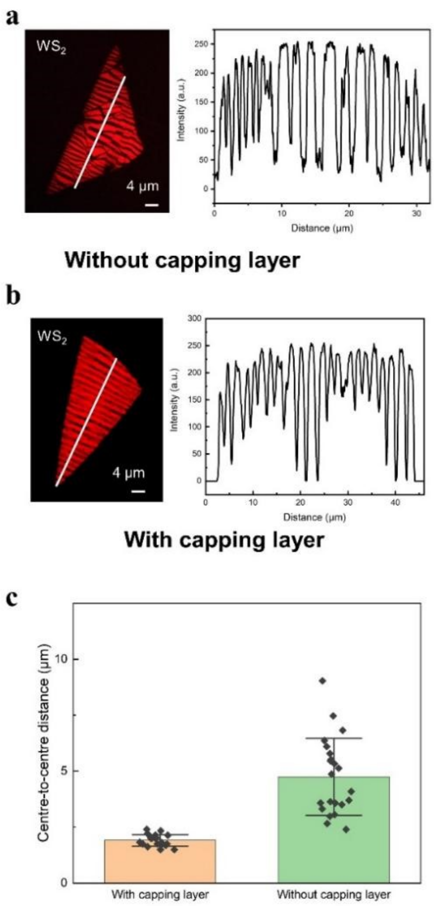

Figure S2. (a) Intensity profile along the white line of the fluorescence image of a WS_2 monolayer after cold drawing without a capping layer. (b) Intensity profile along the white line of the fluorescence image of a WS_2 monolayer after cold drawing with a capping layer. (c) Mean (bar) and standard deviation (error bar) of the center-to-center distance of each fragment calculated from the intensity profiles in (a) and (b).

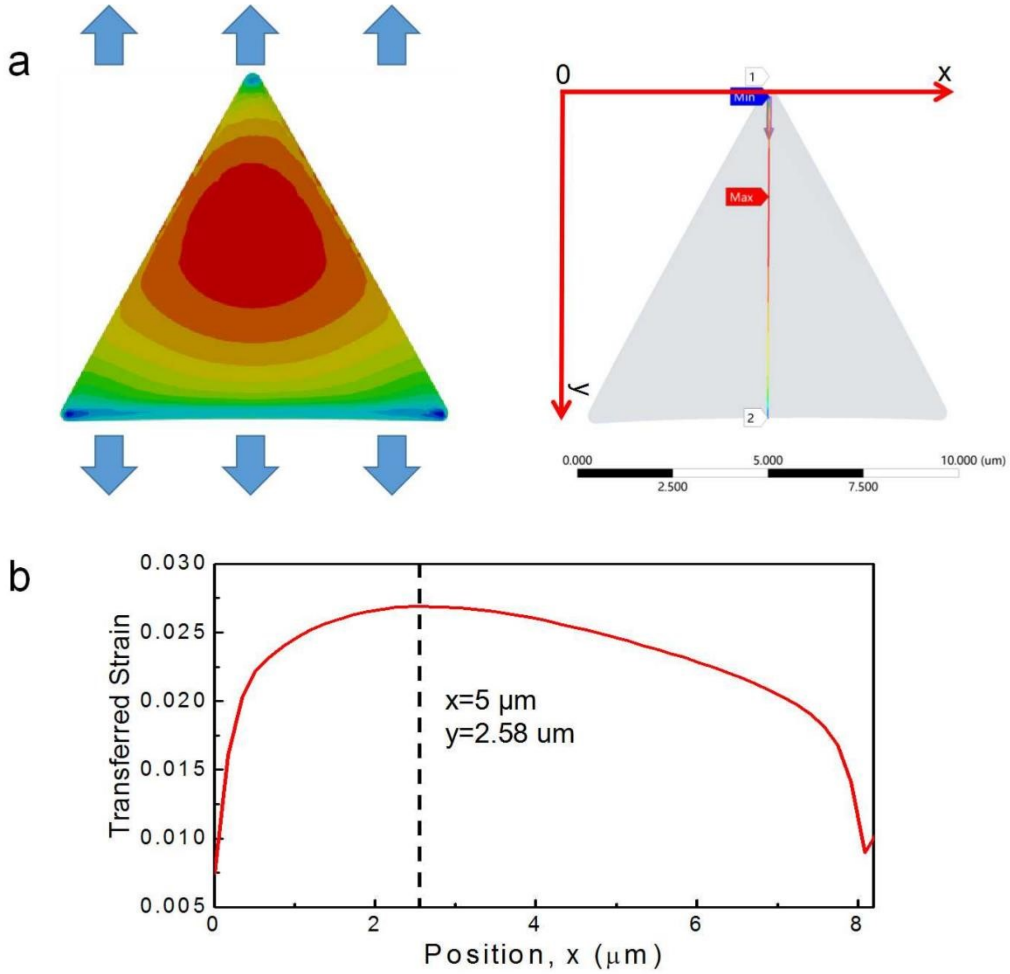

Figure S3. (a) Distribution of the transferred strain in the WS_2 flake with the size of 10 μm (substrate drawing strain: 0.1, PC/WS_2/PMMA structure). (b) Distribution of the transferred strain in the WS_2 flake along the direction of the tensile loading (*y* axis) at the substrate drawing strain of 0.1. The maximum transferred strain is located at *x*=5 μm, *y*=2.58 μm.

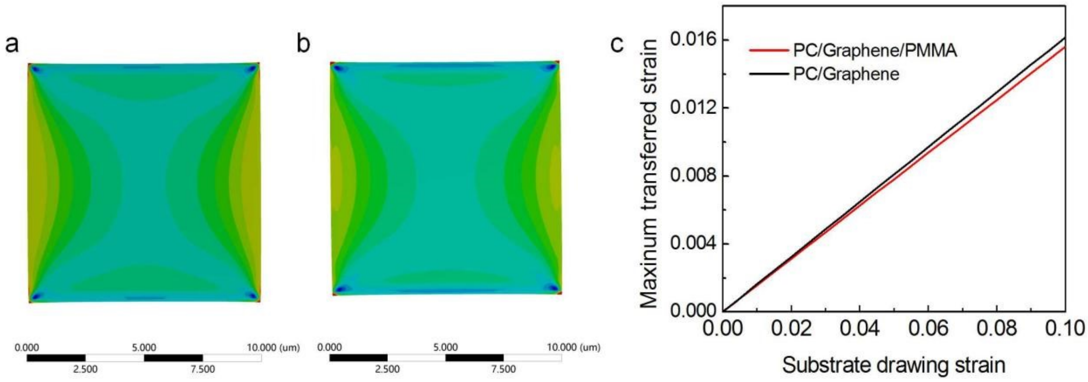

Figure S4. (a-b) Distributions of the transferred strain in single crystalline monolayer graphene with the size of 10 μm (substrate drawing strain: 0.1) for PC/WS_2 and PC/WS_2/PMMA structures, respectively. (c) Effect of PMMA capping layer on the maximum transferred strain in monolayer graphene.

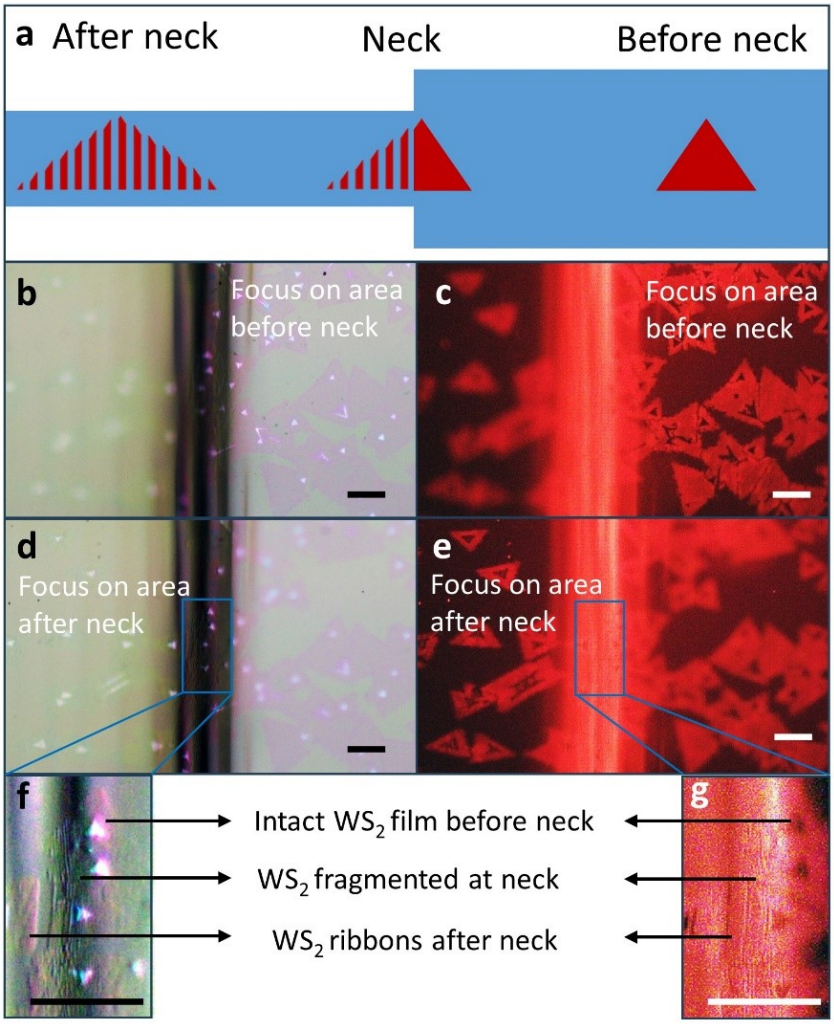

Figure S5. (a) Schematic of the morphological characteristics of WS_2 film during cold drawing. Ordered fragmentation on the WS_2 film happens only at the neck front. The WS_2 films fragmented into ordered nanoribbons at the area after neck propagation, while intact WS_2 films were observed in the before-neck area. Optical and fluorescence images of the area before the neck (b, c) and after the neck (c, d). Insets (f, g) show the enlargement of the ordered fragmentation site. Scale bars, 25 μm.

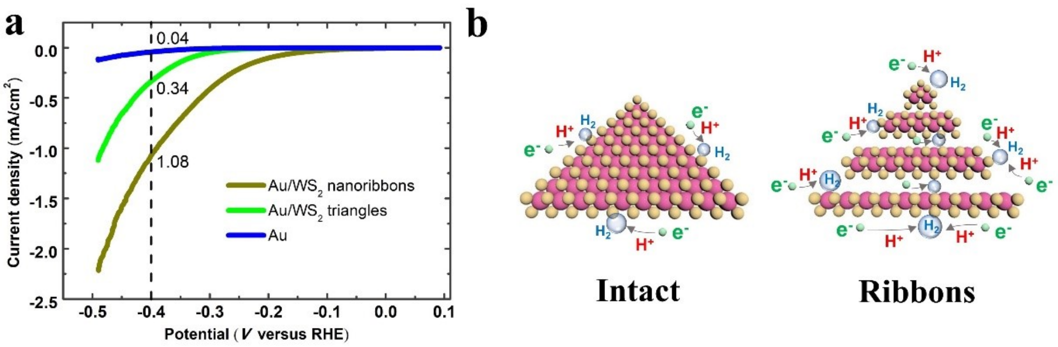

Figure S6. (a) Hydrogen evolution reaction (HER) polarizing curves for supporting Au (blue), monolayer WS_2 triangles (green), and monolayer WS_2 ribbons (yellow). (b) Schematic illustrations of the enhancement for HER by the increased edges of WS_2 ribbons.

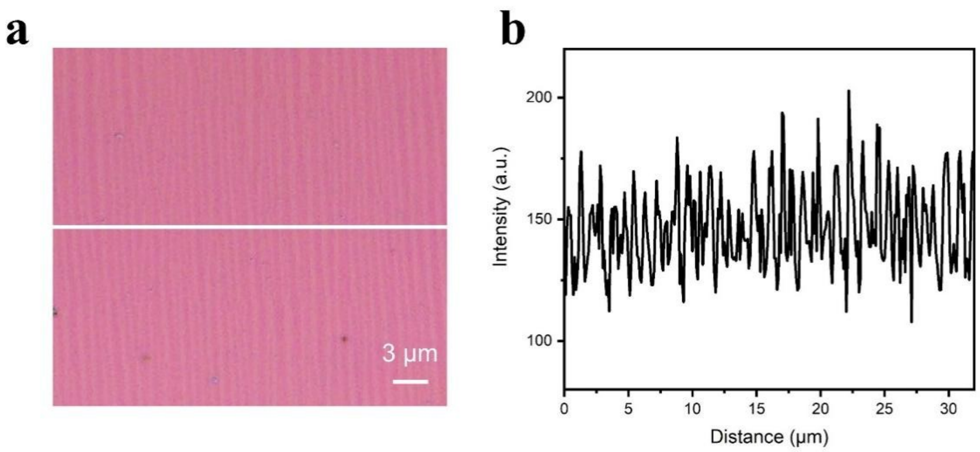

Figure S7. (a) Optical image of the graphene ribbons fabricated via cold drawing. (b) Intensity profile along the white line in (a).

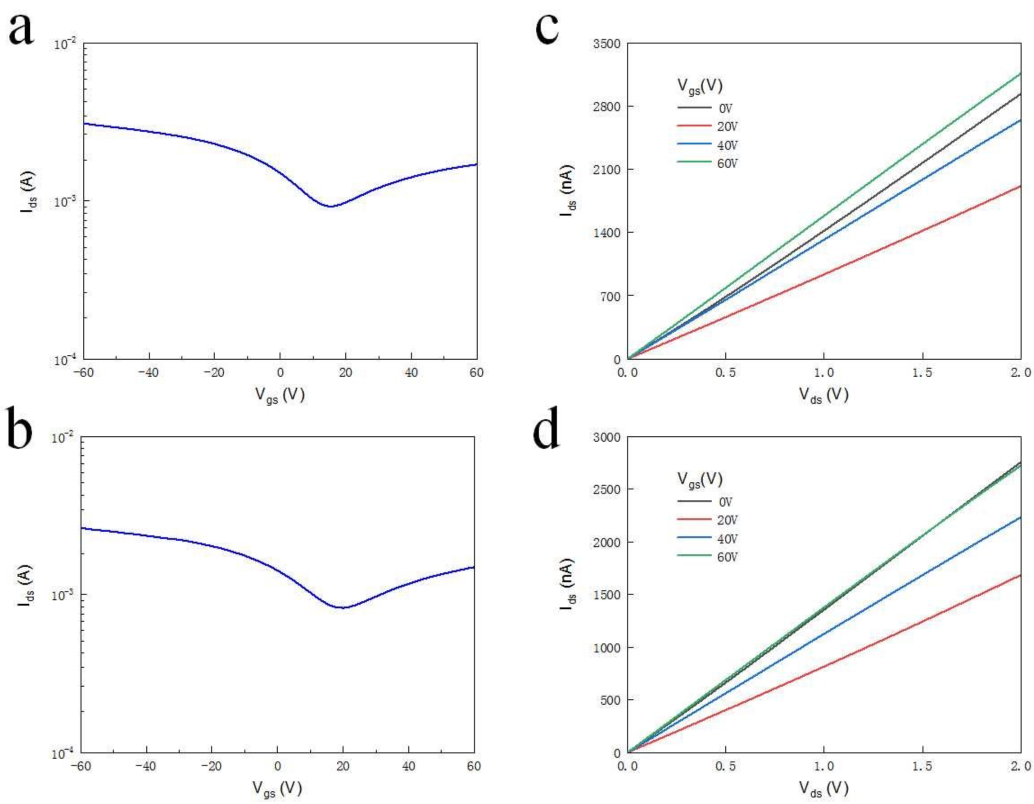

Figure S8. Electrical properties of the fabricated graphene ribbons. (a, b) Transfer characteristics ($I_{ds}-V_{gs}$) of the FETs at V_{ds} = 1 V for devices 1 and 2. (c, d) Output characteristics ($I_{ds}-V_{ds}$) of the FETs under gate voltages ranging from 0 to 60 V for devices 1 and 2.

Table S1. Resistances of Au electrodes during the experiments.

		Before stretching	In stretching	After stretching
Sample 1	Parallel to stretching	3.0Ω	3.6 Ω	3.4 Ω
	Perpendicular to stretching	4.5 Ω	5.1 Ω	4.9 Ω
Sample 2	Parallel to stretching	5.6 Ω	6.1 Ω	5.8 Ω
	Perpendicular to stretching	1.9 Ω	2.5 Ω	2.1 Ω

Mechanical modeling

In view of the small interfacial displacements in the elastic deformation stage of the cold drawing process, linear interfacial shear laws are introduced to describe the constitutive behavior at interfaces 1 and 2, that is,

$$\tau_1 = \kappa_1 \delta_1, \qquad (S1)$$

$$\tau_2 = \kappa_2 \delta_2, \qquad (S2)$$

where τ_i, δ_i and κ_i are the interfacial shear stress, relative displacement and stiffness coefficients at interface $i\ (i = 1,2)$, respectively. As the substrate is deformed uniformly with a stretch ratio of λ, the relative displacement at interface 1 can be written as

$$\delta_1 = z_f - \lambda Z \qquad (S3)$$

and similarly, for the interface 2,

$$\delta_2 = z_c - z_f. \qquad (S4)$$

In Eqs. (S3) and (S4), Z and z denote any positions in the initial and deformed configurations of the corresponding component. The subscripts 'f' represents the film and 'c' the capping layer. Note that in cases of large deformation, the interfacial shear might reach a plateau as interfacial sliding initiates [1], even followed by a damage process [2-4].

For an infinitesimal element in the deformed film/capping layer, the corresponding equilibrium conditions yield

$$\frac{d\sigma_f}{dz_f} = \frac{\tau_1 - \tau_2}{h_f}, \qquad (S5)$$

$$\frac{d\sigma_c}{dz_c} = \frac{\tau_2}{h_c}, \qquad (S6)$$

respectively. Here, h denotes the thickness of the layer and σ the axial Cauchy stress in the layer. In the elastic deformation stage, linear elastic constitutive relationships can be applied to the thin film and capping layer. Therefore, the deformed elements in the thin layers can be related to their initial counterparts through

$$dz_f = \frac{1}{s_f} dZ, \qquad (S7)$$

$$dz_c = \frac{1}{s_c} dZ \qquad (S8)$$

where $s_f = \exp\left(-\sigma_f / E_f\right)$ and $s_c = \exp\left(-\sigma_c / E_c\right)$. From Eqs. (S1)-(S6) we obtain

$$\frac{ds_f}{dZ} = \frac{1}{E_f h_f}\left[\kappa_1(z_c - z_f) - \kappa_2(z_f - \lambda Z)\right] \qquad (S9)$$

and

$$\frac{ds_c}{dZ} = -\frac{1}{E_c h_c}\kappa_1(z_c - z_f). \qquad (S10)$$

The closed-form solution to the stress distributions σ_f, σ_c (or equivalently s_f, s_c) and deformed configurations z_f, z_c can thus be solved from Eqs. (S7)-(S10), together with appropriate boundary conditions. Since the length of interface 3 between the substrate and capping layer is much larger than the film feature size in experiment, the interfacial shear is assumed to have reached a constant strength $\bar{\tau}_3$ away from the free edges. For the simplified model without interface 3 (boxed in **Figure 3a**), we first consider two limiting cases: the one with $\bar{\tau}_3 = 0$ and the one with $\bar{\tau}_3 \to \infty$, which have boundary conditions on the capping layer:

$$s_c(L) = 1 \qquad (S11a)$$

and

$$z_c(L) = \lambda L, \qquad (S11b)$$

respectively, with L being initial half length of the film. The other boundary conditions are the same for both cases:

$$z_f(0) = 0, \qquad (S12)$$

$$z_c(0) = 0, \qquad (S13)$$

$$s_f(L) = 1. \qquad (S14)$$

Although it is challenging to find analytic solutions to the boundary value problems, approximate numerical solutions can be readily obtained using the shooting method.

We suggest an approximate method to determine the critical configurations which have an interfacial shear strength $\bar{\tau}_3$ between the two limits and the same maximum film tension as that in the system without a capping layer. We assume that the deformation of the portion of the capping layer in contact with the substrate is only due to the load transfer at interface 3. Therefore, the critical interfacial shear strength $\bar{\tau}_3$ to prevent premature fracture of the film can be calculated as

$$\bar{\tau}_3 = \frac{\sigma_c^L h_c}{L_c - L} \qquad (S15)$$

where the axial stress σ_c^L of capping layer at $Z = L$ should be solved from the model with the boundary conditions Eqs. (S12) - (S14) and

$$s_f(0) = \min\left\{\exp\left[(\lambda - 1)\left(\frac{1}{\cosh \beta L} - 1\right)\right], \quad \exp\left(-\sigma_s / E_f\right)\right\} \qquad (S16)$$

where $\beta = \sqrt{\kappa_1 / E_f h_f}$ is a constant and σ_s denotes the fracture strength of the film. In Eq. (S16), we adopted the results from the classical shear lag theory [5]. Example calculations on the critical value of $\bar{\tau}_3$ result in a 6.3% difference from FE simulation results, showing the effectiveness of the proposed method to evaluate the critical configurations.

References:

[1] D. Li, Z. Wang, M. Chen, L. Wei, H. Gao, H, *J. Mech. Phys. Solids* **2022**, 159, 104726.

[2] Y. L. Chen, B. Liu, X. Q. He, Y. Huang, K. C. Hwang, *Compos. Sci. Technol.* **2010**, 70, 1360.

[3] G. Guo, Y. Zhu, *J. Appl. Mech.* **2015**, 82, 031005.

[4] F. R. Poblete, Y. Zhu, *J. Mech. Phys. Solids* **2019**, 127, 191.

[5] H. L. Cox, *Br. J. Appl. Phys.* **1952**, *3*, 72.